

Quantifying the fractal dimension and morphology of individual atmospheric soot aggregates

Pang, Yun'er; Wang, Yuanyuan; Wang, Zhicheng; Zhang, Yinxiao; Liu, Lei; Kong, Shaofei; Liu, Fengshan; Shi, Zongbo; Li, Weijun

DOI:
[10.1029/2021JD036055](https://doi.org/10.1029/2021JD036055)

License:
None: All rights reserved

Document Version
Peer reviewed version

Citation for published version (Harvard):

Pang, Y, Wang, Y, Wang, Z, Zhang, Y, Liu, L, Kong, S, Liu, F, Shi, Z & Li, W 2022, 'Quantifying the fractal dimension and morphology of individual atmospheric soot aggregates', *Journal of Geophysical Research: Atmospheres*, vol. 127, no. 5, e2021JD036055. <https://doi.org/10.1029/2021JD036055>

[Link to publication on Research at Birmingham portal](#)

Publisher Rights Statement:

An edited version of this paper was published by AGU. Copyright (2022) American Geophysical Union.

General rights

Unless a licence is specified above, all rights (including copyright and moral rights) in this document are retained by the authors and/or the copyright holders. The express permission of the copyright holder must be obtained for any use of this material other than for purposes permitted by law.

- Users may freely distribute the URL that is used to identify this publication.
- Users may download and/or print one copy of the publication from the University of Birmingham research portal for the purpose of private study or non-commercial research.
- User may use extracts from the document in line with the concept of 'fair dealing' under the Copyright, Designs and Patents Act 1988 (?)
- Users may not further distribute the material nor use it for the purposes of commercial gain.

Where a licence is displayed above, please note the terms and conditions of the licence govern your use of this document.

When citing, please reference the published version.

Take down policy

While the University of Birmingham exercises care and attention in making items available there are rare occasions when an item has been uploaded in error or has been deemed to be commercially or otherwise sensitive.

If you believe that this is the case for this document, please contact UBIRA@lists.bham.ac.uk providing details and we will remove access to the work immediately and investigate.

Abstract

26 The complex morphology of soot aggregates is a major source of uncertainty in evaluating
27 their warming effects in the atmosphere. Fractal dimension (D_f) is a key parameter in quantifying
28 the morphology of soot particles. Previous studies are mostly based on manual identification of
29 soot monomers in electron microscopic images and are hard to provide comparable results in
30 determination of D_f . Here we develop a novel image recognition technique to automatically
31 determine the D_f of individual soot aggregates from electron microscopy images. The novel
32 method has been shown to be able to trace the small change of the soot D_f from an urban tunnel
33 (1.61 ± 0.19) to its exit (1.70 ± 0.15). By applying this new method, we show a substantial
34 difference in average D_f of soot particles emitted from vehicles (1.66 ± 0.17) than from biomass
35 burning (1.75 ± 0.18) and coal burning (1.76 ± 0.18). Average D_f of soot from an urban atmosphere
36 (1.77 ± 0.18) is close to that from biomass and coal combustion but much lower than that from a
37 rural atmosphere (1.85 ± 0.13). In summary, the new technique provides an automatic, accurate
38 and reliable quantification of soot morphology (D_f), enabling an improved understanding of soot
39 aging processes and a more accurate modeling of soot impact on their climate.

Plain Language Summary

41 Soot particles play a significant role in global climate warming by affecting the radiative
42 balance at both global and regional scales. A key challenge of evaluating the warming effects of
43 soot particle is to quantify their complex morphology. We for the first time developed a novel
44 image recognition technique to quantify the morphology of individual soot particles on electron
45 microscopy and collected a large amount of soot particles from various combustion sources and
46 ambient atmosphere. We compared the new method with previous methods and found aging
47 process of soot particles from tunnel entrance to exit. Our results show substantial differences in
48 the morphology of soot particles from different sources and allow us to better model the soot
49 impact on the climate.

50

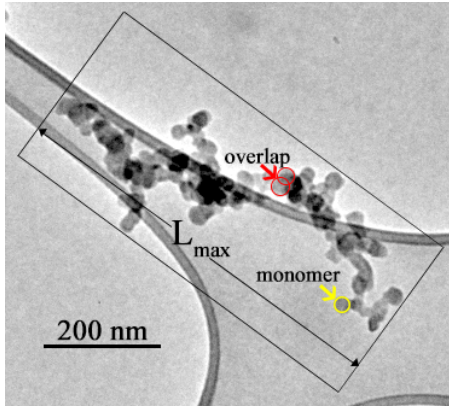
51

52

53 **1 Introduction**

54 Soot, also known as black carbon (BC), is a typical aerosol particle. It plays the major role of
55 light-absorbing carbonaceous component of fine particles and forms during the incomplete
56 combustion of biomass and fossil fuels (Bond et al., 2013). Soot particle has been considered as
57 the second largest anthropogenic radiative forcer in the present-day climate after CO₂ (Boucher
58 et al., 2013). It plays a significant role in global warming by affecting the radiative balance at
59 both global and regional scales (Moffet & Prather, 2009; Peng et al., 2016; Ramanathan &
60 Carmichael, 2008; Teng et al., 2019). Because of their light absorption capacity, a large number
61 of soot particles in polluted air above the planetary layer (PBL) can depress the PBL height and
62 further deteriorate surface air quality (Ding et al., 2016). Soot particles are also constitute of
63 covalently bound clusters of polycyclic aromatic hydrocarbon (PAHs) and other hydrocarbons
64 that contribute to soot surface growth and have detrimental impacts on human health and
65 environment (Johansson et al., 2018; Pendergrass & Hartmann, 2012).

66 Individual soot particles display very complex morphological structures (Y. Y. Wang et al.,
67 2017). Studies show that soot particles are chain-like aggregates that are composed of tens to
68 thousands of nearly spherical monomers with diameters of 5-50 nm (China et al., 2013; Li et al.,
69 2003) and a certain degree of overlap and necking between touching monomers (Figure 1). Up to
70 now, it has remained a challenge to quantify the complex fractal morphology of individual soot
71 particle (China et al., 2013; Ishimoto et al., 2019). Though we can visualize the real morphology
72 of individual soot particles through various advanced electron microscopes, the lack of methods
73 that efficiently quantify the fractal morphology directly from the electron microscopic images
74 prevents the morphological data of real soot particles conversion to numerical shape models.
75 However, the numerical shape models of soot particles are essential to accurately simulate their
76 optical properties and quantify their climate effects in the atmospheric models (K. Adachi et al.,
77 2007; van Poppel et al., 2005; Y. Wang et al., 2021b).



78

79 **Figure 1.** An example of a transmission electron microscope (TEM) image of one soot aggregate.
 80 The rather thick gray curving lines are the lacey carbon supporting substrates.

81

82 The fractal dimension (D_f) has been widely used as a key parameter to describe the fractal
 83 morphology of soot particles (Brasil et al., 1999; Oh & Sorensen, 1997) and the following three
 84 methods have been developed and applied to calculate the D_f of soot particles based on electron
 85 microscopic images in the past decades. The first one is the box counting method. This method
 86 can detect the boundary of individual soot particle but its computation process is based on the
 87 number of pixels occupying, either entirely or partially, the boundary of soot particle on the
 88 transmission electron microscope (TEM) image (Wentzel et al., 2003). The second one is an
 89 ensemble method which has been developed by Brasil et al. (1999) and Oh and Sorensen (1997).
 90 The ensemble method estimates D_f manually from a power law fit of a scatter plot of
 91 morphology parameters of soot particles shown in the electron microscopic images. Recent
 92 studies utilizing the ensemble method have shown that D_f falls with the range of 1.53-1.92 for
 93 soot particles freshly emitted by wildfire (China et al., 2013) and is about 1.80 for soot particles
 94 collected in polluted air (Y. Y. Wang et al., 2017). According to the works mentioned above, we
 95 noticed that the fractal properties were quantitatively analyzed based on the self-similarity of an
 96 ensemble of soot particles rather than individual soot particles, which remains an obstacle to
 97 simulating individual soot models numerically and to better observing the aging process of soot
 98 particles in the atmosphere. Thus, an VISUAL BASIC program was developed by Xiong and
 99 Friedlander (2001), which can derive D_f of individual soot particle though the power law
 100 relationship between the location of monomers and the number of monomers in a soot particle.
 101 However, this requires the operator to spend 20-30 mins to manually measure the required

102 parameters of each monomer of individual soot aggregates, which is both tedious and time-
103 consuming. Until now, there is no efficient method to quantify the D_f of individual soot particles
104 on electron microscopy. To increase the efficiency in determining the morphology of individual
105 soot particles on electron microscopic images and to take the advantage of recent rapid progress
106 in computer language and image recognition techniques, it is highly desirable to develop an
107 automated method to accurately determine the D_f of individual soot particles.

108

109 **2 Methods**

110 2.1 Sampling Site

111 Detailed information of sampling sites of both field observations and laboratory measurements
112 is summarized in Table S1. For the tunnel site, the Wujing road Tunnel is in Tianjin, which is a
113 highly urbanized and densely populated city in northern China with populations of 15 million.
114 Detailed information about the tunnel can be found in Song et al. (2018). Three sampling sites
115 are located at the entrance (34 m from the inlet), midpoint (584 m from the inlet), and exit (115
116 m from the outlet) of the tunnel. We also collected particles from diesel buses, heavy-duty diesel
117 vehicles and light-duty gasoline vehicles on dynamometers of two motor vehicle inspection
118 facilities in Nanjing, China. For the particles from biomass burning and coal combustion, we
119 performed both field observations and laboratory experiments. Detailed information is
120 summarized in Table S1. For the urban sampling sites, we selected three cities to represent
121 typical urban environments: Beijing in the North China Plain (NCP), Hangzhou in the Yangtze
122 River Delta (YRD) of southern China, and Hong Kong in the Pearl River Delta (PRD) of
123 southern China. These three cities are all metropolises in China with populations of 21.5, 9.8 and
124 7.5 million, respectively. The sampling sites in Beijing, Hangzhou, and Hong Kong were located
125 in China University of Mining and Technology (Beijing), Zhejiang University, and Hong Kong
126 Polytechnic University, respectively. The two rural sites of Yucheng and Lin'an were definite
127 background sites, far from any cities and surrounded by small villages, hilly lands and cultivated
128 lands.

129 2.2 Aerosol sampling and analysis

130 Individual particle samples were collected for 30-180 s on copper (Cu) transmission electron
131 microscopic (TEM) grids covered with carbon film (lacey carbon, SPI supplies lacey carbon

132 coated, 300 mesh copper grids, 3 mm). A two-stage cascade impactor (DKL-2, Genstar
133 Electronic Technology, China) with a 0.5 mm and 0.3 mm diameter jet nozzle at air flow rate of
134 1.0 L/min was used to collect aerosol samples. A TEM (JEOL JEM-2100, Japan) coupled with
135 an energy-dispersive X-ray spectrometer (EDS, INCA X-MaxN 80T, Oxford Instruments,
136 United Kingdom) was used to obtain the image and elemental composition of individual
137 particles. Because the distribution of aerosol particles of different size was not uniform on the
138 TEM grids, we chose 3-4 areas from the center to edge of the sampling spot and analyzed all the
139 particles to represent different sized particles.

140 2.3 Fractal dimension analysis of soot particles

141 The fractal dimension of soot particle is an important morphological parameter and is
142 mathematically related to other parameters through the scaling law (Brasil et al., 1999; Köylü et
143 al., 1995; Oh & Sorensen, 1997):

$$144 \quad N = K_g \left(\frac{R_g}{R_0} \right)^{D_f} \quad (1)$$

145 where D_f is fractal dimension, R_g is the radius of gyration, K_g is fractal prefactor, R_0 represents
146 average radius of the monomer, and N is the number of the primary monomers of the aggregate.
147 The scaling law is the theoretical basis used in the box counting, ensemble, and soot parameters
148 methods considered in this study.

149 2.4 Box Counting Method

150 The box counting method, also called the nested square method, is a well-developed method to
151 determine the D_f of individual particles (Lottin et al., 2013). In this study, we use FracLac, which
152 is a plugin for ImageJ software (<http://imagej.nih.gov/ij/>) to implement the box counting method.
153 The details of the box counting method are provided in the Supporting Information (SI).

154 2.5 Ensemble Method

155 The ensemble method, also known as the collective method based on the scaling law, has
156 received increasing attention in recent years (China et al., 2014; Y. Y. Wang et al., 2017). This
157 method first requires parameters of a number of soot aggregates and finally provides a mean D_f
158 of all the particles in the sample through manual efforts. In this method, the fractal dimension
159 and prefactor can be derived from the linear fit of a scatter plot of $\log(N)$ versus $\log(R_g/R_0)$
160 based on equation (1). In addition to the D_f , the total number of monomers (N) (Figure 1) and

161 overlap parameter (δ) of individual soot particles can also be estimated in the ensemble method
 162 through equations (2) and (3):

$$163 \quad N = k_a \left(\frac{A_a}{A_p} \right)^\alpha \quad (2)$$

$$164 \quad \delta = 2a/l \quad (3)$$

165 where A_a is the projected area of soot aggregate, A_p is the mean projected area of monomers, k_a
 166 is a constant, and α is an empirical projected area exponent. The overlap parameter (δ)
 167 dependent on the monomer radius (a) and the distance between the centers of two touching
 168 monomers (l) (Oh & Sorensen, 1997). If $\delta=1$, the monomers are in point contact. In addition, R_g
 169 in equation (1) can be estimated from the maximum projected length of an aggregate (L_{\max})
 170 (Figure 1), using the following relationship (Brasil et al., 1999):

$$171 \quad L_{\max}/2R_g = 1.50 \pm 0.05 \quad (4)$$

172 Here, L_{\max} is an easily measurable parameter based on the TEM image, which can simplify the
 173 calculation process. As shown in Figure S2, the soot particles collected in the urban tunnel
 174 (sample-A) have a mean $D_f = 1.70$.

175 2.6 Soot parameters method

176 Based on equation (1), we developed a novel and accurate algorithm, named the soot
 177 parameters (SP) method, programmed with the Python language and based on the scaling law
 178 and image recognition technology. The SP method can automatically identify individual soot
 179 particles and their monomers in the TEM image and further compute D_f and other morphological
 180 parameters (e.g., radius of gyration, fractal prefactor, radius of the monomer) for one single soot
 181 particle. Then the SP contains the scaling law equation to further compute D_f of individual soot
 182 particle. Here we developed this automated method based on equation (1) without any
 183 assumptions for parameters. Figure S3 shows the step-by-step procedure of this approach using a
 184 soot particle collected from traffic emissions as an example.

185 In the code of the SP method, the Otsu algorithm (Kapur et al., 1985; Otsu, 1979), Opening
 186 and Closing algorithm (Pitas, 2000), Canny Edge detection (CED) (Canny, 1986), and Circular
 187 Hough Transform (CHT) (Duda & Hart, 1972; Hough Paul, 1962) have been used to analyze the
 188 features of different particles. The background of TEM images varies sample by sample and
 189 image by image due to the differences among the types of particles, carbon film, and the
 190 magnification/intensity setting. We first apply Otsu algorithm to implement the image

191 segmentation and search for a threshold that minimizes the intraclass variances of the segmented
 192 image. At the first step, the 16 bits images were converted to 8 bits, as shown in Figure S3b. In
 193 order to further eliminate irregularities on the image background, a morphological smoothing
 194 operator, called Opening and Closing method, was applied in the SP. At the second step, the
 195 CED was applied to detect outlines of monomers of soot aggregates. As shown in Figure S3c, the
 196 CED detected the outline of monomers according to the intensity and gradient of the image,
 197 which means more contour curves would be detected in darker and more concentrated areas, then
 198 result in more monomers recognized during the next process of CHT. Before the CHT, the
 199 Python code would display a pop-up window to require selecting the region of interest to
 200 distinguish the target soot particle and substrate of carbon films, as shown in Figure S3d. After
 201 selection, we got a series of curve fragments of target soot particle, which can be put into the
 202 CHT for the monomers detection (Figure S3e). The CHT algorithm is good at detecting circles
 203 and has been used to detect soot particle in previous studies (Grishin et al., 2012; Kook et al.,
 204 2016). We improved the algorithm of CHT by re-recognizing the monomers twice in large
 205 monomers and small monomers, respectively, to ensure that the recognition result is consistent
 206 with the human observation. Finally, a PNG image and a CSV file that contains one big data of
 207 all the morphology information (e.g., monomer positions, number of monomers, radius of
 208 gyration, radius of monomers, and fractal dimension) can be produced. The SP method can
 209 automatically complete all the steps without any manual operations except Step 4 shown in
 210 Figure S3d.

211 The basic theory of the SP method is the scaling relationship between the morphology
 212 information and the number of monomers in fractal aggregates. So we can obtain the location (x ,
 213 y) and radius of each monomer (Figure S3f) and the total number of monomers (N) in individual
 214 soot particles, which can be used to further derive the radius of gyration (R_g) according to
 215 equation (5) (Oh & Sorensen, 1997).

$$216 \quad R_g = \left(\frac{1}{\sum_0^N m_i} \sum (m_i r_i^2) \right)^{\frac{1}{2}} \quad (5)$$

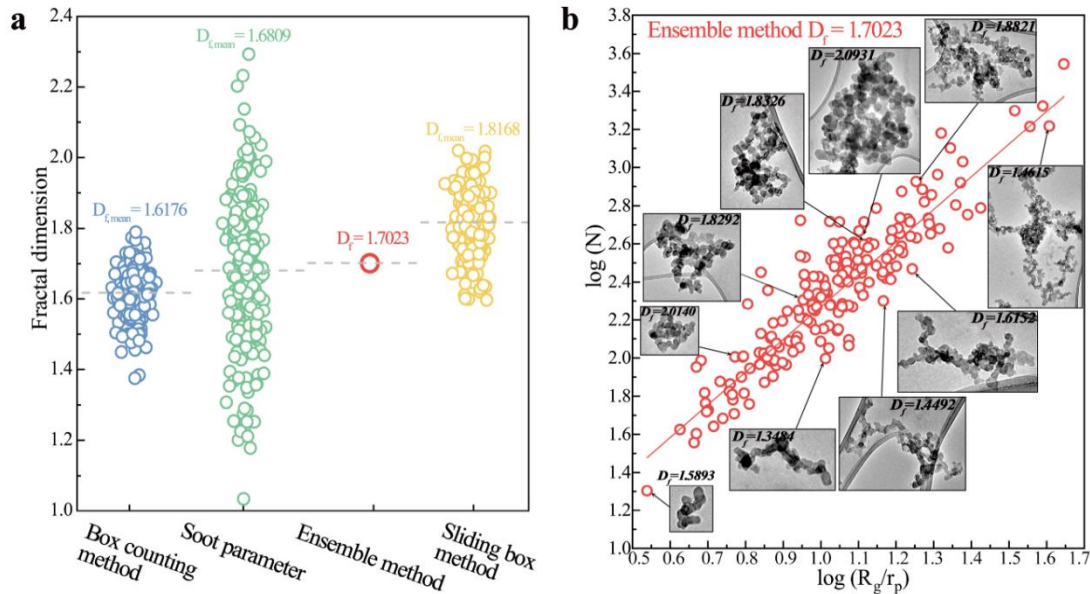
217 where r_i is the position vector of the center of the i^{th} monomer, m_i is the mass of the i^{th} monomer.
 218 After we obtain the value of R_g , number of monomers and radius of individual soot particle
 219 through the SP method, D_f can be derived from the slope of the plot $\log(N)$ versus $\log(R_g/R_0)$
 220 based on the equation (1).

221 Note that the monomers overlap in the three-dimensional structure which can cause darkened
222 color from gray to dark on the projection of soot particles in TEM images. The image
223 recognition technique is applied in the SP to detect more monomers in the darker and more
224 complex part of the particles in the process of image recognition algorithm. Moreover, the
225 method can deal with the embedded soot particles in which monomers are engulfed into other
226 materials and not visible from the TEM images (Figure S4a). When processing such invisible
227 part, the SP method packs this part of particles using the monomers with the average monomer
228 diameter and overlapping rate of the recognized monomers, as shown in Figure S4b.

229 **3 Results and Discussion**

230 3.1 Comparisons of soot fractal dimension

231 Here we compared two box counting methods (i.e., box counting method and sliding box
232 method), SP method, and an ensemble method, using the same set of images that includes 255
233 soot particles in tunnel sample-A (see Table S2). Figure 2a shows that the average D_f values of
234 soot aggregates from the four methods range from 1.63 to 1.83. The ensemble method yields $D_f =$
235 1.70 for the soot particles collected in the tunnel, which generally agrees with D_f calculated by
236 the same method for soot emitted from sources, namely 1.70-1.78 from the spark ignition
237 vehicles engines (Chakrabarty et al., 2006), 1.70-1.85 from diesel (Soewono & Rogak, 2011;
238 Wentzel et al., 2003), 1.52-1.94 from road side (China et al., 2014), and 1.70 ± 0.04 from pre-
239 mixed ethane and oxygen gas combustion (Chakrabarty et al., 2007). Moreover, $D_f = 1.70$ of soot
240 particles collected in the tunnel fall into the range of freshly emitted soot particles (1.53-1.78)
241 (China et al., 2013) but far less than embedded (fully coated) soot particles (1.9-2.6) (Kouji
242 Adachi et al., 2010; Bambha et al., 2013; Y. Y. Wang et al., 2017) in the urban air. Overall, the
243 measured result is reasonable because the heavy vehicular traffic in the tunnel results in copious
244 amounts of fresh soot particles.



245
 246 **Figure 2.** D_f comparisons of soot particles obtained from different methods. (a): Fractal
 247 dimensions calculated by box counting method, soot parameter (SP), ensemble method, and
 248 sliding box method for the same soot samples collected from traffic emissions in a tunnel. (b):
 249 Fractal dimension calculated by the ensemble method (scatter and the single fitting result on the
 250 top) and SP method (D_f for each soot aggregate in the box). The TEM images of soot particles
 251 and their corresponding D_f derived by the SP are shown.

252
 253 Figure 2a shows that the D_f values from the two box counting methods, 1.62 and 1.82, are the
 254 smallest and the largest among the results of the four methods. Because the computation process
 255 of both box methods are based on the number of pixels rather than the actual size of the TEM
 256 images (see Figure S1), the derived D_f value highly depends on the resolution of each image.
 257 Low resolution images may lead to an overestimation of the projected surface area (Gwaze et al.,
 258 2006), which would then result in inaccuracy of the D_f . In the process of image binarization (see
 259 Figure S1b), the overlapping and the size information of the monomers are lost. Therefore, the
 260 two box counting methods may not be appropriate for aggregates composed of polydisperse
 261 monomers, which are generally the case.

262 The average $D_f = 1.68$ from the SP is very close to $D_f = 1.70$ from the ensemble method. Figure
 263 2b displays various morphologies of soot particles and their corresponding D_f values from the
 264 SP. The SP method not only obtains the average D_f of all the analyzed soot particles but also
 265 distinguishes the D_f of individual soot particles (Figure 2b). The D_f values of soot aggregates

266 collected in the tunnel range in 1.03 to 2.29 by the SP (Figure 2a). The large D_f range of
267 individual soot particles can be attributed to the different aged vehicles emitting different soot
268 structure (China et al., 2014; Dye et al., 2000; Zhu et al., 2005). On urban roads, there are always
269 different types and ages of private cars.

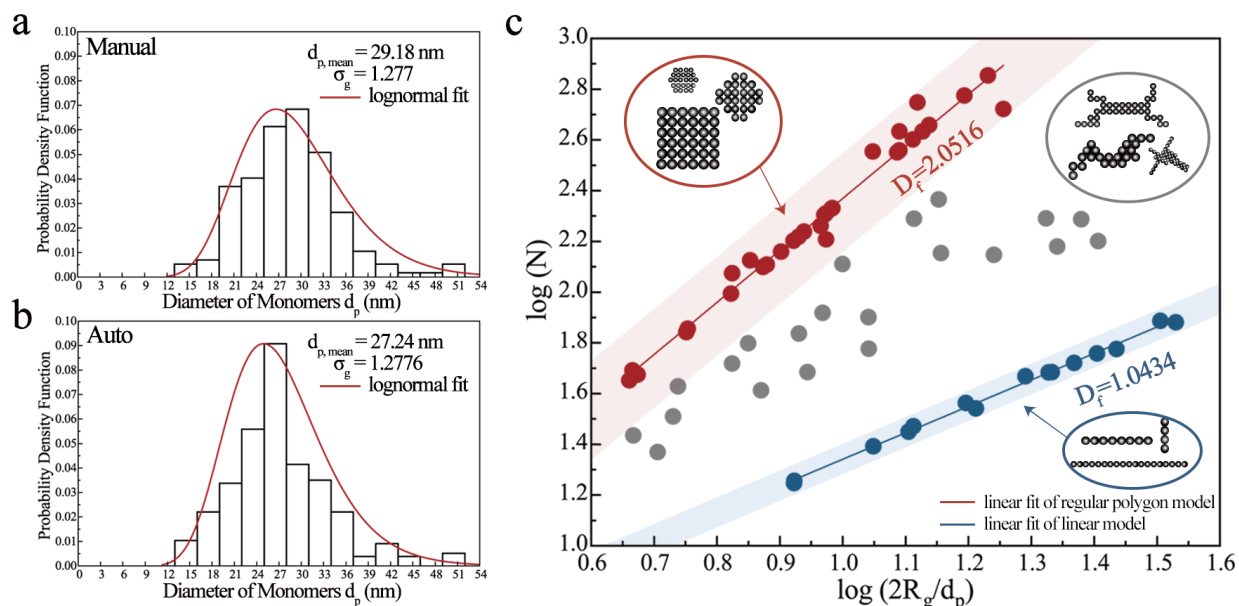
270 Based on their data processing and comparisons of their derived D_f values of soot particles,
271 limitations and advantages of all the four methods were summarized in Table S3. The ensemble
272 method cannot differentiate D_f in individual soot particles. Moreover, k_a and α in equation (2)
273 (see Methods) are widely accepted as empirical values in the literature (China et al., 2013; Oh &
274 Sorensen, 1997), and the estimation of δ in equation (3) is also subject to large uncertainty as we
275 cannot figure out the lattice spacing between every pair of monomers in individual soot
276 aggregate. On the contrary, the SP method can directly measure various parameters (e.g., d_p , R_g ,
277 N and K_g) in equation (5) and (1) and further calculates the D_f of individual soot particles. The
278 key point is that the SP method can accurately identify polydisperse monomers in individual soot
279 particles (see Figure S3), while the ensemble method can only assume the monomers to be same-
280 sized spheres. However, the SP can better recognize TEM images up to now while the ensemble
281 method can also acquire the information from scanning electron microscope (SEM) images. In a
282 word, we conclude that the SP method is superior based on comparisons between the SP and
283 ensemble methods: it is an automated and highly efficient tool to provide the fractal dimensions
284 of individual soot particles in TEM images.

285 3.2 Evaluating the SP method

286 The newly developed SP method consists of image processing and mathematical calculations. It
287 is necessary to evaluate how the D_f from the SP method can precisely represent the fractal
288 morphology of soot aggregates. Firstly, we test the image processing in the SP and quantify the
289 ability of automated measurements. It is well known that the size of soot monomers (d_p) is an
290 important parameter to reflect the aggregate structure of individual soot particles (China et al.,
291 2014) and affect the D_f calculation in equation (1). Here we compare the size distribution of soot
292 monomer in all the soot particles in sample-A from the manual measurements and automated
293 identification from the SP method (Figure 3a, 3b).

294 The size distribution of 48,174 monomers from one big data generated by the SP method
295 shows that the d_p of soot monomer falls in a range of 15-52 nm with a mean size of 27.2 nm,

296 which is close to the manually determined d_p in a range of 14-65 nm with a mean size of 29.2
 297 nm. The monomer d_p from these two approaches in our study is similar to the soot d_p in a range
 298 of 20-40 nm from vehicle emissions of spark ignition engines (Chakrabarty et al., 2006), 26-44
 299 nm from traffic samples in Arizona, and 10-60 nm from a light-duty diesel engine (Zhu et al.,
 300 2005). Moreover, assuming that the d_p satisfies the lognormal size distribution, the values of
 301 geometric standard deviation (σ_g) obtained by the manual and automated measurements are
 302 given in Figure 3a and 3b, which are in good agreement (~ 1.28) (Figure 3a, 3b). The result falls
 303 into a range of 1.11-1.54 for the soot σ_g from ethylene combustion, exhaust of aircraft engines,
 304 vehicle emissions, and wood combustion (Bescond et al., 2014; Chakrabarty et al., 2006; Gwaze
 305 et al., 2006).



306
 307 **Figure 3.** The size distributions of the diameter of monomers (d_p) with the fitted normal
 308 distribution (red lines): (a) Manual measurement from the ensemble method, (b) Automated
 309 measurement from the SP method, (c) The fractal dimension of linear models (blue), regular
 310 polygon models (red), and soot-like models (grey) calculated by the ensemble method.

311
 312 We constructed well-defined standard aggregates with known D_f based on the scaling law
 313 (equation 1). According to the geometric theory, these regular objects have their fixed D_f , i.e., a
 314 line has $D_f = 1$, a planar structure has $D_f = 2$, and a cube has $D_f = 3$. To further validate the SP
 315 accuracy, two types of standard models were generated: linear chain and regular polygon (Figure
 316 3c). Finally, the SP obtains the D_f from 1.00 to 2.01 of 16 linear models and 29 regular polygon

317 models, respectively. This shows that the D_f from the SP method is in good agreement with the
318 expected theoretical values. The ensemble method is also used to obtain D_f at 1.04 and 2.05 for
319 the linear and regular polygon models, respectively (Figure 3c). This result shows that the
320 calculated D_f displays a nearly perfect correlation when we consider the standard models with
321 similar shapes. If we generate an ensemble of particles containing some compact and some
322 chain-like models to mimic the real soot particles with different monomer sizes, these D_f data of
323 individual model particles scatter between the linear and polygon models but cannot be fitted by
324 a linear regression. As a result, the accuracy of the ensemble method is significantly reduced if
325 one sample significantly contains different morphologies of soot particles. In other word, the
326 ensemble method can only work well for self-similar soot particles in the sample that all have
327 similar fractal dimensions. Moreover, the ensemble method cannot provide D_f of individual soot
328 particles. On the contrary, the SP can remedy the drawbacks of the ensemble method and provide
329 us with new insight into the calculation and knowledge of the fractal properties of individual soot
330 particles. Moreover, the SP incorporates the automated image processing capability and thus can
331 process a large number of soot aggregates in a short time.

332 3.3 Morphology characteristics of real soot particles

333 The soot formation process highly depends on the combustion conditions and the types of
334 combustion sources (Buseck et al., 2014; Zhu et al., 2005). As shown in the TEM images (Figure
335 4), the monomers, aggregate size, and fractal properties of individual soot particles vary
336 significantly among the particles even in the same sample (Bond et al., 2013). Hence,
337 quantifying the morphology of individual soot-containing particles is critical to understand the
338 feature of emission sources and the aging process of soot particles (China et al., 2013; Y. Y.
339 Wang et al., 2017). We analyzed the morphology and mixing structure of individual soot-
340 containing particles through transmission electron microscopy (TEM) coupled with energy
341 dispersive X-ray spectroscopy (EDS). EDS can determine elemental composition of soot-
342 containing particle to assist us in selecting the mixing structure categories. We basically judge
343 the mixing structure categories through the TEM observations. It should be noted that the
344 method has been well used in Y. Wang et al. (2021a) through the volume proportion of BC
345 embedded in coating. Based on the TEM/EDS, we simply classified the soot particles into three
346 types: bare-like, partly-coated, and embedded. The bare-like soot is a chain-like aggregate with
347 no or extremely thin organic matter (OM) coating (Figure 4a). The partly-coated soot represents

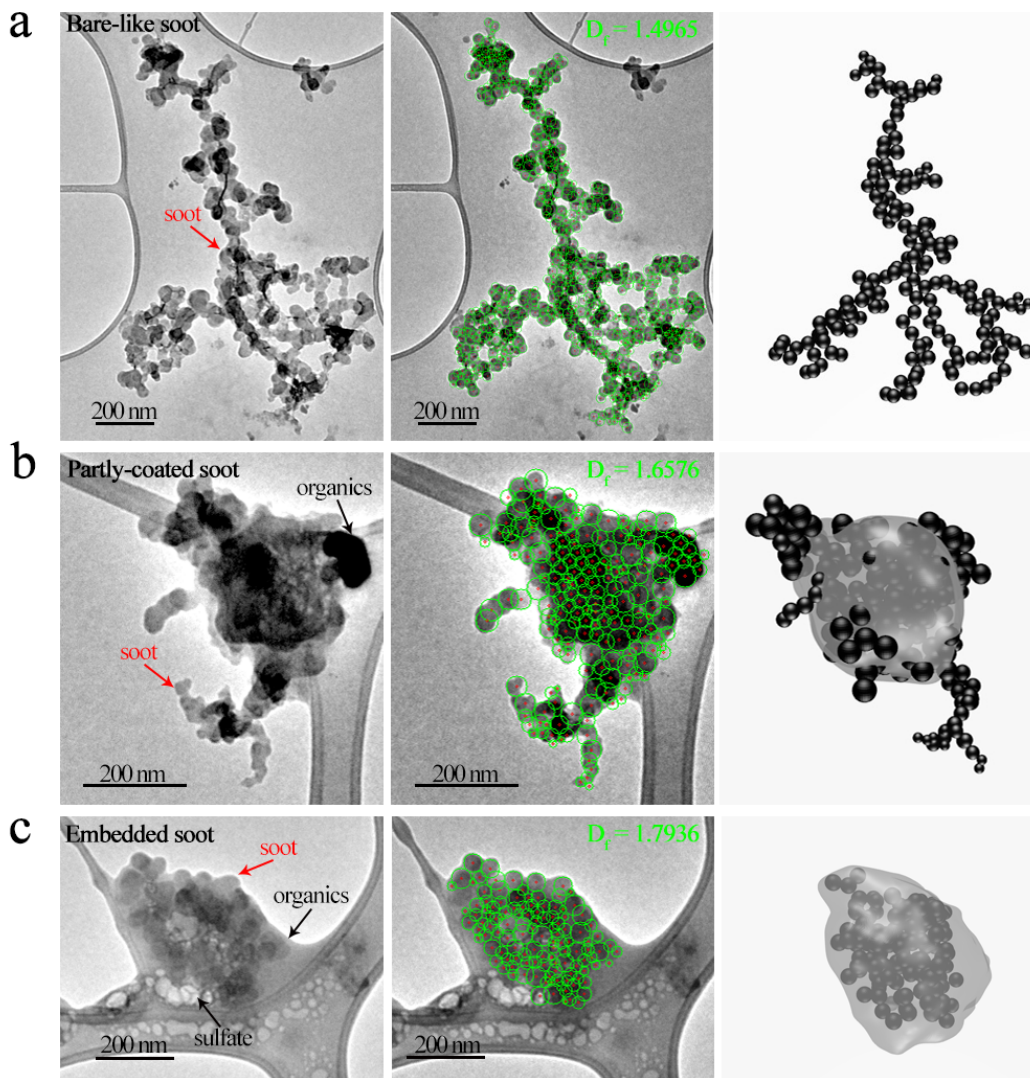
348 a soot particle that is partly mixed with organic or inorganic components (Figure 4b). The
349 embedded soot particle is heavily coated or entirely embedded within other aerosols (Figure 4c).
350 Through the functions of image recognition techniques, the SP method can still obtain
351 parameters of monomers even for soot particles covered by secondary aerosols (e.g., sulfate,
352 nitrate, and organic matter) in TEM images (Figure 4). Figure 4 shows the three different types
353 of soot particles collected from traffic emissions in the tunnel (sample-B) and their D_f calculated
354 by the SP, such as $D_f = 1.50$ of a bare-like, $D_f = 1.66$ of a partly coated, and $D_f = 1.79$ of an
355 embedded soot particle.

356 As the most important parameter to quantify the morphology of soot particles, the D_f plays an
357 important role in the evaluation of the scattering and radiative properties of soot particles (Li Liu
358 & Mishchenko, 2005; Y. Wang et al., 2021b). Figure 4 shows that soot monomers are identified
359 accurately by the green circles in the TEM images. The parameters of position and size of every
360 monomer are used in the calculation of the D_f for each soot aggregate. The number, position,
361 size, and D_f of soot monomers are then used to generate a three-dimensional numerical model of
362 each soot aggregate. Based on parameters such as D_f , k_g , and N of individual soot particles in
363 TEM images and the results from EDS, the structure of a soot aggregate was generated by a
364 tunable algorithm proposed by Filippov et al. (2000) and the detailed information about how to
365 construct the soot models is described by Y. Wang et al. (2021a) and Y. Wang et al. (2021b).
366 Based on their morphological parameters from the SP, we successfully generate for the first time
367 three numerical soot models (Figure 4). Once the numerical soot models are built, they can be
368 further fed to the optical models (e.g. DDA and T-matrix) to calculate the optical properties of
369 soot particles (Kouji Adachi et al., 2010; Kahnert & Devasthale, 2011; Y. Wang et al., 2021b;
370 Zeng et al., 2019).

371 3.4 Quantifying the aging process of soot particles

372 We noticed that the morphology of individual soot particles varied significantly. To trace the
373 aging process and the fractal properties of soot particles, we further measured the D_f of soot
374 particles from the same emission source (see Sample-B, Table S2) using the SP in a tunnel.
375 Figure S5 shows that D_f varies with the location in the tunnel, such as 1.61 ± 0.19 in the tunnel
376 entrance, 1.66 ± 0.19 in the tunnel midpoint, and 1.70 ± 0.15 in the tunnel exit. The increased D_f
377 from the tunnel entrance to the tunnel exit is consistent with the change of mixing structure of

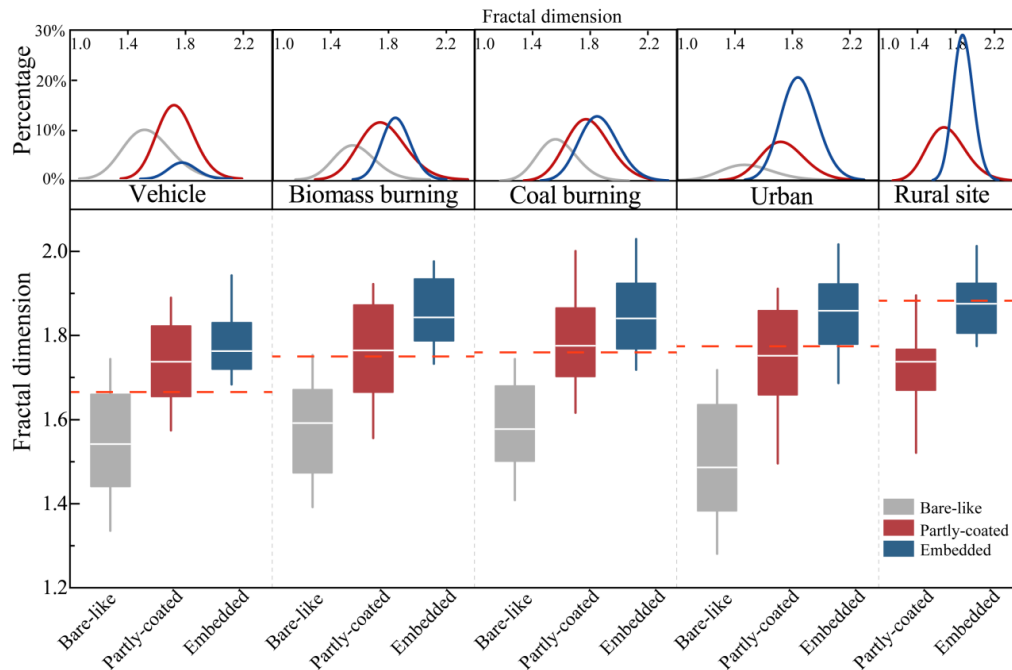
378 soot particles (Figure S5), suggesting that some soot particles become slightly aged in the 1554
 379 m tunnel. Based on the sampling time, the aging ratio is estimated to be 0.18/h (aging ratio = $(D_{f, \text{exit}} - D_{f, \text{entrance}})/\Delta t$) in the tunnel based on the D_f changes.



381
 382 **Figure 4.** TEM images of three typical soot particles (first column), their corresponding SP
 383 processed images (second column), and their three-dimension models (third column). (a) One
 384 fresh soot particle collected at the tunnel entrance and its $D_f = 1.50$, (b) Partly-coated soot
 385 particle collected at the tunnel midpoint and its $D_f = 1.66$, (c) Embedded soot particle collected at
 386 the tunnel exit and its $D_f = 1.79$. The 3D soot numerical models are generated from a tunable
 387 algorithm (Filippov et al., 2000) and one EMBS developed by Y. Wang et al. (2021a) based on
 388 the D_f of soot particles and the numbers and sizes of monomers.

389

390 1,370 soot particles from three combustion sources — vehicles, biomass burning, and coal
 391 burning — and five ambient sampling sites (e.g., Beijing city, Hangzhou city, Hong Kong city,
 392 Lin'an rural site and Yucheng rural site) were analyzed. Figure 5 shows that the average D_f
 393 values of various soot particles are 1.66 for vehicles, 1.75 for biomass burning, 1.76 for coal
 394 burning, 1.77 for urban air, and 1.85 for rural air. The majority soot particles from vehicles,
 395 biomass burning, and coal burning are partly-coated soot particles with the mean D_f of 1.73, 1.77
 396 and 1.79, respectively. The mean D_f values of bare-like soot particles in the corresponding
 397 combustion sources are 1.54, 1.57, and 1.58, respectively (Figure 5). We also found that the
 398 amount of embedded soot particles is nearly the same as that of partly-coated soot particles from
 399 both the biomass burning and coal burning sources, which have the same D_f at 1.86. The high
 400 percentage of organic aerosols emitted from biomass burning and coal burning (Hodshire et al.,
 401 2019; Lei Liu et al., 2017; Zhang et al., 2018) may have contributed to the presence of large
 402 amount of embedded soot particles.



403
 404 **Figure 5.** D_f of three types of soot particles from vehicle exhaust, biomass burning, coal burning,
 405 and from urban and rural ambient air. The white lines in the boxes are the medians, and the red
 406 dashed lines display the mean D_f of soot particles from those sources. Vertical error bars
 407 represent the 90% confidence interval of D_f . The percentages of the three types of soot particles
 408 are shown above the box plots.

409

410 Compared with the soot particles from the combustion sources, the D_f values of soot particles
411 from urban sites (1.77) and rural sites (1.85) were larger, and no bare-like soot particle was
412 found at the remote rural sites. These results suggest that the aging process during the transport
413 from emission sources to ambient air result in more compact soot particles. Coatings of
414 secondary aerosols significantly changed the fractal morphology of soot particles from the chain-
415 like aggregate to more compact one. Moreover, we noticed that the number fraction of embedded
416 soot particles at the rural sites was significantly higher and that they had the highest D_f at 1.88,
417 suggesting that the long-range-transport of aerosol particles could transform the relatively open
418 structure of freshly emitted soot particles to a more compact structure (Khalizov et al., 2009; Pei
419 et al., 2018; Y. Y. Wang et al., 2017).

420 In summary, we provide a novel method to automatically determine the fractal properties of
421 individual soot particles. This method opens a new door for the microscopic characterization of
422 individual soot particles. It will transform the way to characterize the morphology of soot
423 particles and enable a better understanding of the soot aging process.

424

425 **Acknowledgments**

426 **Funding Sources**

427 This work was funded by the National Natural Science Foundation of China (42075096;
428 91844301) and Zhejiang Provincial Natural Science Foundation of China (LZ19D050001).

429 **Author Contributions**

430 Y.P. and W.L. designed this study and wrote the original draft. Y.W. and Y.Z. collected the
431 aerosol particles. Y.P., Z.W., L.L., Y.W. and Y.Z. carried out the laboratory experiments and
432 data analyses. S. K., F. L., and Z.S. interpreted the results and improved the manuscript

433 **Conflict of Interest**

434 The authors declare no conflicts of interest relevant to this study.

435 **Data Availability Statement**

436 Data supporting the results are available in the supporting information. The data presented in this
 437 publication are available online (<https://10.6084/m9.figshare.17871755>). The codes are available
 438 from website <https://doi.org/10.6084/m9.figshare.16393833>

439 References

- 440 Adachi, K., Chung S. H., Buseck P. R. (2010), Shapes of soot aerosol particles and implications for their effects on
 441 climate, *Journal of Geophysical Research: Atmospheres*, 115(D15), D15206, <https://doi.org/10.1029/2009JD012868>
 442 Adachi, K., Chung S. H., Friedrich H., Buseck P. R. (2007), Fractal parameters of individual soot particles
 443 determined using electron tomography: Implications for optical properties, *Journal of Geophysical Research:*
 444 *Atmospheres*, 112(D14), D14202, <https://doi.org/10.1029/2006JD008296>
 445 Bambha, R. P., Dansson M. A., Schrader P. E., Michelsen H. A. (2013), Effects of volatile coatings and coating
 446 removal mechanisms on the morphology of graphitic soot, *Carbon*, 61, 80-96,
 447 <https://doi.org/https://doi.org/10.1016/j.carbon.2013.04.070>
 448 Bescond, A., Yon J., Ouf F. X., Ferry D., Delhaye D., Gaffie D., et al. (2014), Automated Determination of
 449 Aggregate Primary Particle Size Distribution by TEM Image Analysis: Application to Soot, *Aerosol Science and*
 450 *Technology*, 48(8), 831-841, <https://doi.org/10.1080/02786826.2014.932896>
 451 Bond, T. C., Doherty S. J., Fahey D. W., Forster P. M., Berntsen T., DeAngelo B. J., et al. (2013), Bounding the role
 452 of black carbon in the climate system: A scientific assessment, *Journal of Geophysical Research: Atmospheres*,
 453 118(11), 5380-5552, <https://doi.org/10.1002/jgrd.50171>
 454 Boucher, O., D. Randall, P. Artaxo, C. Bretherton, G. Feingold, P. Forster, et al. (2013), Clouds and Aerosols, paper
 455 presented at *Climate Change 2013: The Physical Science Basis. Contribution of Working Group I to the Fifth*
 456 *Assessment Report of the Intergovernmental Panel on Climate Change*, Cambridge Univ. Press, New York.
 457 Brasil, A. M., Farias T. L., Carvalho M. G. (1999), A recipe for image characterization of fractal-like aggregates,
 458 *Journal of Aerosol Science*, 30(10), 1379-1389, [https://doi.org/10.1016/S0021-8502\(99\)00026-9](https://doi.org/10.1016/S0021-8502(99)00026-9)
 459 Buseck, P. R., Adachi K., Gelencsér A., Tompa É., Pósfai M. (2014), Ns-Soot: A Material-Based Term for Strongly
 460 Light-Absorbing Carbonaceous Particles, *Aerosol Science and Technology*, 48(7), 777-788,
 461 <https://doi.org/10.1080/02786826.2014.919374>
 462 Canny, J. F. (1986), A Computational Approach to Edge Detection. In Fischler, et al. (Eds.), *Readings in Computer*
 463 *Vision*, (pp. 679-698), Morgan Kaufmann, San Francisco
 464 Chakrabarty, R. K., Moosmüller H., Arnott W. P., Garro M. A., Slowik J. G., Cross E. S., et al. (2007), Light
 465 scattering and absorption by fractal-like carbonaceous chain aggregates: comparison of theories and experiment,
 466 *Applied Optics*, 46(28), 6990-7006, <https://doi.org/10.1364/AO.46.006990>
 467 Chakrabarty, R. K., Moosmüller H., Arnott W. P., Garro M. A., Walker J. (2006), Structural and Fractal Properties of
 468 Particles Emitted from Spark Ignition Engines, *Environmental Science & Technology*, 40(21), 6647-6654,
 469 <https://doi.org/10.1021/es060537y>
 470 China, S., Mazzoleni C., Gorkowski K., Aiken A. C., Dubey M. K. (2013), Morphology and mixing state of
 471 individual freshly emitted wildfire carbonaceous particles, *Nature Communications*, 4, 2122,
 472 <https://doi.org/10.1038/ncomms3122>
 473 China, S., Salvadori N., Mazzoleni C. (2014), Effect of Traffic and Driving Characteristics on Morphology of
 474 Atmospheric Soot Particles at Freeway On-Ramps, *Environmental Science & Technology*, 48(6), 3128-3135,
 475 <https://doi.org/10.1021/es405178n>
 476 Ding, A. J., Huang X., Nie W., Sun J. N., Kerminen V. M., Petäjä T., et al. (2016), Enhanced haze pollution by
 477 black carbon in megacities in China, *Geophysical Research Letters*, 43(6), 2873-2879,
 478 <https://doi.org/10.1002/2016GL067745>
 479 Duda, R. O., Hart P. E. (1972), Use of the Hough transformation to detect lines and curves in pictures, *Commun.*
 480 *ACM*, 15(1), 11-15, <https://doi.org/10.1145/361237.361242>
 481 Dye, A. L., Rhead M. M., Trier C. J. (2000), The quantitative morphology of roadside and background urban aerosol
 482 in Plymouth, UK, *Atmospheric Environment*, 34(19), 3139-3148, [https://doi.org/10.1016/S1352-2310\(99\)00437-9](https://doi.org/10.1016/S1352-2310(99)00437-9)
 483 Filippov, A. V., Zurita M., Rosner D. E. (2000), Fractal-like aggregates: Relation between morphology and physical
 484 properties, *Journal of Colloid and Interface Science*, 229(1), 261-273, <https://doi.org/10.1006/jcis.2000.7027>

- 485 Grishin, I., Thomson K., Migliorini F., Sloan J. J. (2012), Application of the Hough transform for the automatic
 486 determination of soot aggregate morphology, *Applied Optics*, 51(5), 610-620, <https://doi.org/10.1364/Ao.51.000610>
- 487 Gwaze, P., Schmid O., Annegarn H. J., Andreae M. O., Huth J., Helas G. (2006), Comparison of three methods of
 488 fractal analysis applied to soot aggregates from wood combustion, *Journal of Aerosol Science*, 37(7), 820-838,
 489 <https://doi.org/10.1016/j.jaerosci.2005.06.007>
- 490 Hodshire, A. L., Bian Q., Ramnarine E., Lonsdale C. R., Alvarado M. J., Kreidenweis S. M., et al. (2019), More
 491 Than Emissions and Chemistry: Fire Size, Dilution, and Background Aerosol Also Greatly Influence Near-Field
 492 Biomass Burning Aerosol Aging, *J24*(10), 5589-5611, <https://doi.org/10.1029/2018JD029674>
- 493 Hough Paul, V. C. (1962), *Method And Means For Recognizing Complex Patterns*, edited, HOUGH PAUL V C,
 494 US,
- 495 Ishimoto, H., Kudo R., Adachi K. (2019), A shape model of internally mixed soot particles derived from artificial
 496 surface tension, *Atmos. Meas. Tech.*, 12(1), 107-118, <https://doi.org/10.5194/amt-12-107-2019>
- 497 Johansson, K. O., Head-Gordon M. P., Schrader P. E., Wilson K. R., Michelsen H. A. (2018), Resonance-stabilized
 498 hydrocarbon-radical chain reactions may explain soot inception and growth, *Science*, 361(6406), 997,
 499 <https://doi.org/10.1126/science.aat3417>
- 500 Kahnert, M., Devasthale A. (2011), Black carbon fractal morphology and short-wave radiative impact: a modelling
 501 study, *Atmospheric Chemistry and Physics*, 11(22), 11745-11759, <https://doi.org/10.5194/acp-11-11745-2011>
- 502 Kapur, J. N., Sahoo P. K., Wong A. K. C. (1985), A new method for gray-level picture thresholding using the
 503 entropy of the histogram, *Computer Vision, Graphics, and Image Processing*, 29(3), 273-285,
 504 [https://doi.org/10.1016/0734-189X\(85\)90125-2](https://doi.org/10.1016/0734-189X(85)90125-2)
- 505 Khalizov, A. F., Zhang R., Zhang D., Xue H., Pagels J., McMurry P. H. (2009), Formation of highly hygroscopic
 506 soot aerosols upon internal mixing with sulfuric acid vapor, *I14*(D5),
 507 <https://doi.org/https://doi.org/10.1029/2008JD010595>
- 508 Kook, S., Zhang R. L., Chan Q. N., Aizawa T., Kondo K., Pickett L. M., et al. (2016), Automated Detection of
 509 Primary Particles from Transmission Electron Microscope (TEM) Images of Soot Aggregates in Diesel Engine
 510 Environments, *Sae International Journal of Engines*, 9(1), 279-296, <https://doi.org/10.4271/2015-01-1991>
- 511 Köylü, Ü. Ö., Faeth G. M., Farias T. L., Carvalho M. G. (1995), Fractal and projected structure properties of soot
 512 aggregates, *Combustion and Flame*, 100(4), 621-633, [https://doi.org/10.1016/0010-2180\(94\)00147-K](https://doi.org/10.1016/0010-2180(94)00147-K)
- 513 Li, J., Anderson J. R., Buseck P. R. (2003), TEM study of aerosol particles from clean and polluted marine boundary
 514 layers over the North Atlantic, *Journal of Geophysical Research: Atmospheres*, 108(D6), 4189,
 515 <https://doi.org/10.1029/2002JD002106>
- 516 Liu, L., Kong S., Zhang Y., Wang Y., Xu L., Yan Q., et al. (2017), Morphology, composition, and mixing state of
 517 primary particles from combustion sources — crop residue, wood, and solid waste, *Scientific reports*, 7(1), 5047,
 518 <https://doi.org/10.1038/s41598-017-05357-2>
- 519 Liu, L., Mishchenko M. I. (2005), Effects of aggregation on scattering and radiative properties of soot aerosols,
 520 *Journal of Geophysical Research: Atmospheres*, 110(D11), D11211, <https://doi.org/10.1029/2004JD005649>
- 521 Lottin, D., Ferry D., Gay J. M., Delhaye D., Ouf F. X. (2013), On methods determining the fractal dimension of
 522 combustion aerosols and particle clusters, *Journal of Aerosol Science*, 58, 41-49,
 523 <https://doi.org/10.1016/j.jaerosci.2012.12.009>
- 524 Moffet, R. C., Prather K. A. (2009), In-situ measurements of the mixing state and optical properties of soot with
 525 implications for radiative forcing estimates, *Proceedings of the National Academy of Sciences of the United States of*
 526 *America*, 106(29), 11872-11877, <https://doi.org/10.1073/pnas.0900040106>
- 527 Oh, C., Sorensen C. M. (1997), The effect of overlap between monomers on the determination of fractal cluster
 528 morphology, *Journal of Colloid and Interface Science*, 193(1), 17-25, <https://doi.org/10.1006/jcis.1997.5046>
- 529 Otsu, N. (1979), A Threshold Selection Method from Gray-Level Histograms, *IEEE Transactions on Systems, Man,*
 530 *and Cybernetics*, 9(1), 62-66, <https://doi.org/10.1109/TSMC.1979.4310076>
- 531 Pei, X., Hallquist M., Eriksson A. C., Pagels J., Donahue N. M., Mentel T., et al. (2018), Morphological
 532 transformation of soot: investigation of microphysical processes during the condensation of sulfuric acid and
 533 limonene ozonolysis product vapors, *Atmospheric Chemistry and Physics*, 18(13), 9845-9860,
 534 <https://doi.org/10.5194/acp-18-9845-2018>
- 535 Pendergrass, A. G., Hartmann D. L. (2012), Global-mean precipitation and black carbon in AR4 simulations,
 536 *Geophysical Research Letters*, 39(1), L01703, <https://doi.org/10.1029/2011GL050067>
- 537 Peng, J. F., Hu M., Guo S., Du Z. F., Zheng J., Shang D. J., et al. (2016), Markedly enhanced absorption and direct
 538 radiative forcing of black carbon under polluted urban environments, *Proceedings of the National Academy of*
 539 *Sciences of the United States of America*, 113(16), 4266-4271, <https://doi.org/10.1073/pnas.1602310113>
- 540 Pitas, I. (2000), *Digital Image Processing Algorithms and Applications*, Wiley-Interscience, New York.

- 541 Ramanathan, V., Carmichael G. (2008), Global and regional climate changes due to black carbon, *Nature*
542 *Geoscience*, 1(4), 221-227, <https://doi.org/10.1038/ngeo156>
- 543 Soewono, A., Rogak S. (2011), Morphology and Raman Spectra of Engine-Emitted Particulates, *Aerosol Science and*
544 *Technology*, 45(10), 1206-1216, <https://doi.org/10.1080/02786826.2011.587036>
- 545 Song, C., Ma C., Zhang Y., Wang T., Wu L., Wang P., et al. (2018), Heavy-duty diesel vehicles dominate vehicle
546 emissions in a tunnel study in northern China, *Science of the Total Environment*, 637-638, 431-442,
547 <https://doi.org/10.1016/j.scitotenv.2018.04.387>
- 548 Teng, S., Liu C., Schnaiter M., Chakrabarty R. K., Liu F. (2019), Accounting for the effects of nonideal minor
549 structures on the optical properties of black carbon aerosols, *Atmospheric Chemistry and Physics*, 19(5), 2917-2931,
550 <https://doi.org/10.5194/acp-19-2917-2019>
- 551 van Poppel, L. H., Friedrich H., Spinsby J., Chung S. H., Seinfeld J. H., Buseck P. R. (2005), Electron tomography
552 of nanoparticle clusters: Implications for atmospheric lifetimes and radiative forcing of soot, *Geophysical Research*
553 *Letters*, 32(24), L24811, <https://doi.org/10.1029/2005GL024461>
- 554 Wang, Y., Li W., Huang J., Liu L., Pang Y., He C., et al. (2021a), Nonlinear enhancement of radiative absorption by
555 black carbon in response to particle mixing structure, *Geophysical Research Letters*, 48(24), e2021GL096437,
556 <https://doi.org/https://doi.org/10.1029/2021GL096437>
- 557 Wang, Y., Pang Y., Huang J., Bi L., Che H., Zhang X., Li W. (2021b), Constructing Shapes and Mixing Structures
558 of Black Carbon Particles With Applications to Optical Calculations, *Journal of Geophysical Research:*
559 *Atmospheres*, 126(10), e2021JD034620, <https://doi.org/10.1029/2021JD034620>
- 560 Wang, Y. Y., Liu F. S., He C. L., Bi L., Cheng T. H., Wang Z. L., et al. (2017), Fractal Dimensions and Mixing
561 Structures of Soot Particles during Atmospheric Processing, *Environmental Science & Technology Letters*, 4(11),
562 487-493, <https://doi.org/10.1021/acs.estlett.7b00418>
- 563 Wentzel, M., Gorzawski H., Naumann K. H., Saathoff H., Weinbruch S. (2003), Transmission electron
564 microscopical and aerosol dynamical characterization of soot aerosols, *Journal of Aerosol Science*, 34(10), 1347-
565 1370, [https://doi.org/https://doi.org/10.1016/S0021-8502\(03\)00360-4](https://doi.org/https://doi.org/10.1016/S0021-8502(03)00360-4)
- 566 Xiong, C., Friedlander S. K. (2001), Morphological properties of atmospheric aerosol aggregates, *Proceedings of the*
567 *National Academy of Sciences of the United States of America*, 98(21), 11851-11856,
568 <https://doi.org/10.1073/pnas.211376098>
- 569 Zeng, C., Liu C., Li J., Zhu B., Yin Y., Wang Y. (2019), Optical Properties and Radiative Forcing of Aged BC due to
570 Hygroscopic Growth: Effects of the Aggregate Structure, *Journal of Geophysical Research: Atmospheres*, 124(8),
571 4620-4633, <https://doi.org/10.1029/2018JD029809>
- 572 Zhang, Y., Yuan Q., Huang D., Kong S., Zhang J., Wang X., et al. (2018), Direct Observations of Fine Primary
573 Particles From Residential Coal Burning: Insights Into Their Morphology, Composition, and Hygroscopicity,
574 *Journal of Geophysical Research: Atmospheres*, 123(22), 12,964-912,979, <https://doi.org/10.1029/2018JD028988>
- 575 Zhu, J., Lee K. O., Yozgatligil A., Choi M. Y. (2005), Effects of engine operating conditions on morphology,
576 microstructure, and fractal geometry of light-duty diesel engine particulates, *Proceedings of the Combustion*
577 *Institute*, 30(2), 2781-2789, <https://doi.org/https://doi.org/10.1016/j.proci.2004.08.232>

578